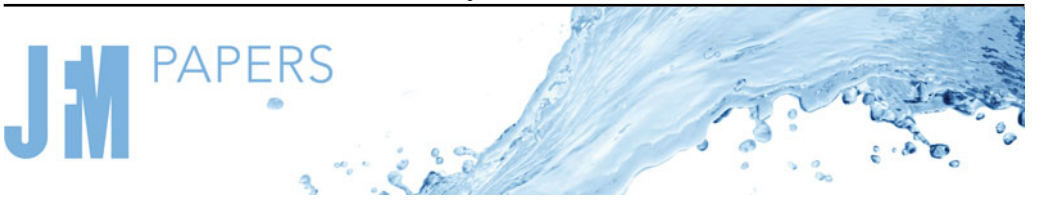
J. Fluid Mech. (2026), *vol.* 1045, A60, doi:10.1017/jfm.2026.12196



Bypass transition beneath internal solitary waves in turbulent boundary layers

Andrés Posada-Bedoya[1], **Jason Olsthoorn**[1] **and Leon Boegman**[1]

[1]Department of Civil Engineering, Queen's University, Kingston, ON K7L 3N6, Canada

Corresponding author: Andrés Posada-Bedoya, 21afpb@queensu.ca

(Received 2 April 2026 UTC; revised 25 July 2026 UTC; accepted 18 September 2026 UTC)

Process-based studies of the transition to turbulence beneath internal solitary waves (ISWs) have typically assumed a laminar bottom boundary layer (BBL) and two-dimensional flow. In natural environments, however, ISWs often propagate over turbulent three-dimensional BBLs. Here, we perform three-dimensional high-resolution spectral numerical simulations of periodic ISWs of depression at momentum-thickness Reynolds numbers representative of laboratory ($Re_{ISW} = 300$) and lake ($Re_{ISW} = 900$) scale conditions to examine how ambient turbulence modifies the transition to turbulence beneath ISWs. When the ambient flow is laminar, this transition is governed by a modal instability. At $Re_{ISW} = 300$, the instability generates localised vortices that subsequently break down, while at $Re_{ISW} = 900$ it produces sustained vortex shedding and a turbulent wake in the lee of the wave. In contrast, when the ambient flow is turbulent, the modal pathway is bypassed. Free-stream turbulence excites near-wall streamwise streaks (Klebanoff modes) beneath the front shoulder of the wave, which amplify, undergo secondary instability and break down into turbulent bursts. The resulting turbulence develops upstream of the modal-instability region. With increasing Reynolds number and stronger ambient turbulence, the onset of turbulence shifts progressively toward the ISW trough. These results show that ambient turbulence triggers a bypass mechanism fundamentally different from the modal-instability-driven transition in laminar environments. By suppressing the modal instability and shifting turbulence generation closer to the wave trough, bypass transition provides an explanation for field observations that cannot be reconciled with laminar-transition models. Accurate prediction of near-bed turbulence and sediment transport in natural environments therefore requires accounting for bypass transition.

Key words: transition to turbulence, turbulent boundary layers, solitary waves

© The Author(s), 2026. Published by Cambridge University Press. This is an Open Access article, distributed under the terms of the Creative Commons Attribution licence (https://creativecommons.org/licenses/by/4.0/), which permits unrestricted re-use, distribution and reproduction, provided the original article is properly cited.

https://doi.org/10.1017/jfm.2026.12196 Published online by Cambridge University Press

1. Introduction

Internal solitary waves (ISWs) are among the most energetic features of stratified lakes and oceans. Their balance between nonlinear steepening and dispersion (Helfrich & Melville 2006) enables them to develop large amplitudes and travel long distances with minimal change in shape. Their large amplitudes generate strong near-bed currents that can drive turbulence, sediment resuspension and bedform evolution, making ISW-driven bottom boundary layers (BBLs) an important component of coastal and shelf dynamics (Helfrich & Melville 2006; Boegman & Stastna 2019). Consequently, ISW–BBL interactions have been the subject of extensive laboratory, numerical and field investigation over the past three decades (e.g. Bogucki & Redekopp 1999; Diamessis & Redekopp 2006; Stastna & Lamb 2008; Carr *et al.* 2008; Aghsaee & Boegman 2015; Zulberti *et al.* 2020; Trowbridge *et al.* 2025).

Despite this substantial body of work, important discrepancies remain across process-based studies and field observations. Laboratory experiments and numerical simulations typically consider a laminar upstream boundary layer and predict transition through shear-instability-driven vortex shedding in the adverse pressure-gradient region behind the wave trough (Stastna & Lamb 2002; Diamessis & Redekopp 2006; Carr *et al.* 2008; Aghsaee *et al.* 2012; Sakai *et al.* 2020*a*; Posada-Bedoya *et al.* 2024). As a result, the flow typically remains laminar under the wave trough, and turbulence generation and sediment resuspension are expected to occur in the wake of the wave (Aghsaee & Boegman 2015; Posada-Bedoya *et al.* 2025*a*). This behaviour is consistent with some field observations that show near-bed maxima in the sediment concentrations near the trailing edge of the wave, likely driven by the shear-instability-driven vortex-shedding transition, for example on the California inner shelf (Johnson *et al.* 2001; Becherer *et al.* 2020), in the Mid-Atlantic Bight 'Mud Patch' (Bogucki *et al.* 2005) and at Dongsha Atoll in the South China Sea (Trowbridge *et al.* 2025). In contrast, field measurements on the Australian continental shelf (Zulberti *et al.* 2020) and the Portuguese shelf (Quaresma *et al.* 2007) have reported enhanced turbulence within the favourable pressure-gradient region, peaking directly under the trough. These observations are accompanied by peak near-bed sediment concentrations occurring near or immediately beneath the trough and by an absence of clear shear-instability signatures, challenging the conventional interpretation of ISW-driven transition via shear-instability-driven vortex shedding. The origin of these contrasting behaviours remains unresolved.

A key distinction between the field observations of Quaresma *et al.* (2007) and Zulberti *et al.* (2020) and most field (Bogucki *et al.* 2005; Becherer *et al.* 2020; Trowbridge *et al.* 2025), laboratory (Carr *et al.* 2008; Aghsaee & Boegman 2015; Posada-Bedoya *et al.* 2025*a*) and numerical (Stastna & Lamb 2002, 2008; Diamessis & Redekopp 2006) studies is the presence of a thick nepheloid layer maintained by an ambient turbulent BBL with a well-developed inertial subrange preceding the ISWs. In contrast, laboratory and numerical studies typically assume laminar upstream conditions, whereas many field observations reporting turbulence in the lee of the wave show low near-bed sediment concentrations before the arrival of the ISW. Motivated by this discrepancy, Sakai *et al.* (2020*b*) hypothesised that incorporating pre-existing turbulence into the BBL could reconcile these differences between laboratory-scale studies and field observations.

We address this hypothesis using high-resolution three-dimensional (3-D) spectral numerical simulations of ISW-driven BBLs with both laminar and turbulent upstream conditions at Reynolds numbers representative of laboratory and lake scales. Our objective is to identify the mechanisms and coherent structures governing transition and determine how pre-existing turbulence modifies the ISW–BBL dynamics, thereby assessing whether

https://doi.org/10.1017/jfm.2026.12196 Published online by Cambridge University Press

it can explain the contrasting behaviour reported in field observations. This work provides the first direct numerical investigation of ISW-driven boundary-layer transition in the presence of ambient turbulence.

2. Theoretical background

An ISW-driven BBL experiences alternating regions of favourable and adverse pressure gradients (FPGs and APGs) ahead of and behind the wave trough, respectively. The APG region induces near-bed flow reversal, which produces an inflection point in the velocity profile that is often linearly unstable (Verschaeve & Pedersen 2014; Posada-Bedoya *et al.* 2024). At finite amplitude, this instability forms a street of vortices, providing a pathway to turbulence through vortex shedding and subsequent breakdown into smaller-scale motions (e.g. Sakai *et al.* 2020*a*,*b*). This sequence represents the classical transition scenario beneath an ISW and is an example of an 'orderly' transition to turbulence (Herbert 1988; Kleiser & Zang 1991), the well-established paradigm for laminar BBL transition. Hereafter, we refer to this 'orderly' transition pathway as *modal instability* since it is driven by the growth of the most unstable mode of the BBL flow.

An alternative pathway arises in the presence of ambient perturbations. In this case, transition may occur through a 'bypass' mechanism, in which free-stream vortical disturbances directly perturb the boundary layer (Durbin & Wu 2007; Zaki 2013). Due to shear sheltering (Hunt & Durbin 1999), only low-frequency disturbances penetrate the BBL, where they amplify into elongated streamwise velocity streaks, commonly referred to as Klebanoff modes (Klebanoff 1971). These streaks grow through the lift-up mechanism described by Landahl (1980), distorting the initially laminar flow. As they amplify, they develop inflectional profiles in the wall-normal and spanwise directions, triggering secondary instabilities that generate turbulent spots (Zaki 2013). These spots subsequently grow, merge and form a fully turbulent boundary layer farther downstream. Hereafter, we refer to this transition pathway as a *bypass transition*.

Within this framework, we define a *laminar environment* as one in which the BBL upstream of the ISW is laminar. Conversely, a *turbulent environment* denotes one where turbulent fluctuations are present in the near-bed region ahead of the ISW, in the form of *free-stream turbulence* (FST). Importantly, the FST is distinct from the background low-level noise that is always present in the field. In the present set-up, this FST originates from the turbulent wake generated by preceding ISWs. A periodic domain causes each wave to encounter the wake left by the previous wave, providing a controlled framework for investigating bypass transition.

3. Methods

3.1. *Problem definition*

We consider periodic ISWs of depression propagating in a 3-D channel with quasi-two-layered density stratification defined with a hyperbolic tangent profile:

$$\bar{\rho}(z) = \rho_0 - \frac{\Delta\rho}{2}\tanh\left(\frac{z - z_{pyc}}{h_{pyc}}\right), \tag{3.1}$$

where $\rho_0 = 1000\,\mathrm{kg\ m^{-3}}$ is a reference density and $\Delta\rho$ is the density difference across a pycnocline of half-thickness $h_{pyc} = 2H/35$ centred at a height $z_{pyc} = 31H/35$, with $\Delta\rho/\rho_0 = 120/1000$, z positive upwards and H is the total depth. This set-up is the 3-D extension of the two-dimensional (2-D) simulations by Posada-Bedoya *et al.* (2024).

https://doi.org/10.1017/jfm.2026.12196 Published online by Cambridge University Press

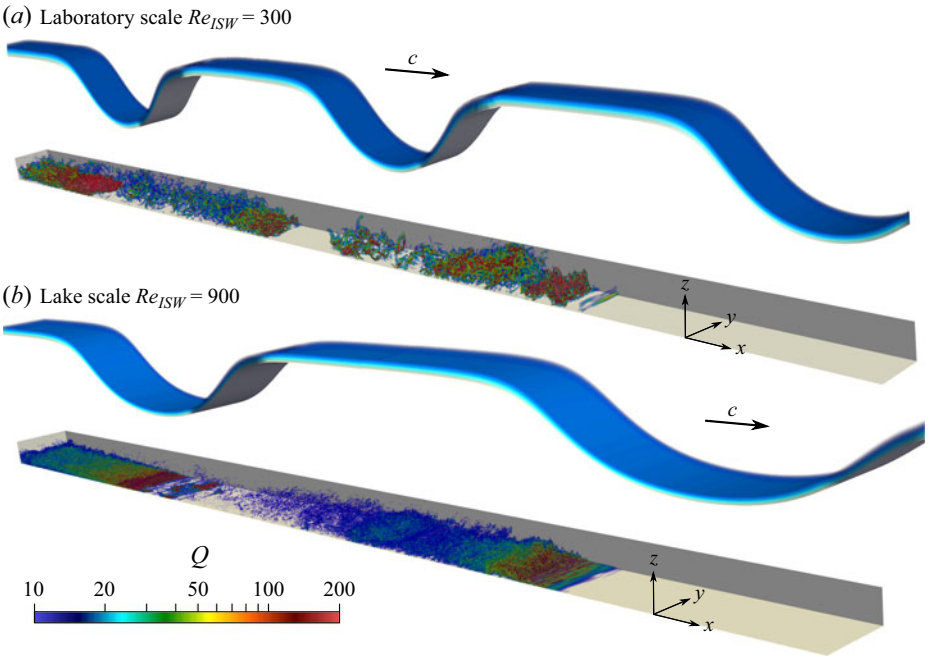


Figure 1. Set-up of the numerical simulations. Contours of density and near-bed Q criterion at the (a) laboratory scale ($Re_{ISW} = 300$) and (b) lake scale ($Re_{ISW} = 900$). Waves propagate to the right. This is a schematic representation constructed by stitching together snapshots from different times, each containing only a single ISW.

The periodic streamwise configuration allows the simulation of ISW–BBL interactions under both laminar and turbulent upstream conditions (figure 1). The first wave propagates through an initially laminar environment, while subsequent waves encounter the turbulent wake left by preceding waves.

The relevant non-dimensional parameters for the BBL instability are the momentum-thickness Reynolds number and the normalised pressure gradient computed from the inviscid ISW-induced velocity field (Aghsaee *et al.* 2012):

$$Re_{ISW} = U_2\sqrt{\frac{L_w}{\nu(U_2 + c)}}, \qquad P_{ISW} = (U_2 + c)\frac{U_2}{L_w g'}, \tag{3.2}$$

where c is the ISW propagation speed, U_2 is the absolute value of the maximum horizontal velocity at the wave trough, $g' = g\Delta\rho/\rho_0$ is the reduced gravity, g is the gravitational constant and ν is the kinematic viscosity. The horizontal half-wavelength is

$$L_w = \frac{1}{a}\int_{-\infty}^{\infty} \eta_p \mathrm{d}x, \tag{3.3}$$

where η_p is the vertical displacement of the pycnocline and a is the wave amplitude.

We simulated two cases (table 1). Case I represents a typical laboratory-scale ISW ($Re_{ISW} = 300$) and is the 3-D extension of case B1 in Posada-Bedoya *et al.* (2024). Case II represents an ISW in a lake or a shallow coastal ocean ($Re_{ISW} = 900$) and is the 3-D extension of case C1 in Posada-Bedoya *et al.* (2024). At laboratory scale (Carr *et al.* 2008; Aghsaee & Boegman 2015; Zahedi *et al.* 2021; Posada-Bedoya *et al.* 2025*a*), $Re_{ISW} = 300$ corresponds to waves with $a \approx 0.17$ m, $L_w \approx 1$ m, $c \approx 0.36$ m s^{-1} and

https://doi.org/10.1017/jfm.2026.12196 Published online by Cambridge University Press

Case	Re_{ISW}	L_y/H	$N(z^+<9)$	Δx^+	Δy^+	Δz^+_{wall}	$N_x \times N_z \times N_y$	Simulation time (t/T)	Wall-clock time† (days core-years^{-1})
Case I	300	0.23	16	7.3	7.2	0.045	4096 × 512 × 128	8.2	68/95
Case IA	300	0.60	16	7.3	7.2	0.045	4096 × 512 × 256	1.8	32/45
Case II	900	0.11	7	22.2	21.8	0.27	8192 × 512 × 128	1.4	59/82
S&S	—	—	10	20.0	6.7	1.0	1000 × 120 × 120	—	—
SDJ	310	0.15	27	8.2	4.6	0.027	12 288 × 480 × 128	—	—
A&S	246‡	—	16	20.7	6.2	0.9	384 × 160 × 128	—	—
V&Z	—	—	—	8.1	6.8	0.4	2049 × 129 × 129	—	—
B&D	347‡	—	—	30.0	12.2	2.15	1024 × 128 × 128	—	—

Table 1. Simulation parameters. Simulation time (t/T) is reported as the number of periodic ISW passages through the domain ($T = 3L_w/c$). Grid resolutions in wall units (+) are indicated at the location of the maximum friction coefficient. In all present cases, $P_{ISW} = 0.116$ and $a/H = 0.37$. † Wall-clock time running on 512 cores in the Compute Ontario clusters of the Digital Research Alliance of Canada. ‡ Momentum thickness Reynolds number. S&S: Spalart & Strelets (2000), SDJ: Sakai *et al.* (2020*a*), A&S: Alam & Sandham (2000), V&Z: Vaughan & Zaki (2011), B&D: Bose & Durbin (2016).

$U_2 \approx 0.21$ m s^{-1}. These waves propagate along a quasi-two-layered stratification ($\Delta\rho = 120$ kg m^{-3} and $z_{pyc} = 0.057$ m) in a $H = 0.5$ m deep flume. In comparison, at field scale, $Re_{ISW} = 900$ corresponds to waves with $a \approx 4$ m, $L_w \approx 36$ m, $c \approx 0.36$ m s^{-1} and $U_2 \approx 0.13$ m s^{-1}. These waves propagate along a quasi-two-layered stratification ($\Delta\rho = 3$ kg m^{-3} and $z_{pyc} = 3$ m) in $H = 20$ m deep lake or coastal ocean. This is of similar scale to ISWs observed on the California inner continental shelf (e.g. Johnson *et al.* 2001; Becherer *et al.* 2020), lakes (Thorpe *et al.* 1972; Farmer 1978; Boegman *et al.* 2003; Dorostkar *et al.* 2017), the St. Lawrence River estuary (Bourgault *et al.* 2014) and Knight Inlet (Farmer & Armi 1999).

As in Posada-Bedoya *et al.* (2024), both simulated waves ($Re_{ISW} = 300$ and $Re_{ISW} = 900$) had identical kinematic and pressure-gradient parameters ($P_{ISW} = 0.11$), differing only in the fluid viscosity and corresponding Reynolds number. To verify that the results were independent of the spanwise domain width, we performed an additional simulation (case IA) identical to case I but with a spanwise domain three times wider.

3.2. *Numerical set-up*

We numerically solved the incompressible Navier–Stokes equations under the Boussinesq approximation:

$$\frac{\partial \boldsymbol{u}}{\partial t} + \boldsymbol{u}\cdot\nabla\boldsymbol{u} = -\frac{1}{\rho_0}\nabla p - g\frac{\rho}{\rho_0}\hat{k} + \nu\nabla^2\boldsymbol{u}, \tag{3.4}$$

$$\frac{\partial \rho}{\partial t} + \boldsymbol{u}\cdot\nabla\rho = \kappa\nabla^2\rho, \tag{3.5}$$

$$\nabla\cdot\boldsymbol{u} = 0, \tag{3.6}$$

where $\boldsymbol{u}$ is the velocity vector, ∇ is the gradient operator, t is time, p is pressure, ρ is the fluid density and κ is the molecular diffusivity. We considered $Pr = \nu/\kappa = 1$, which does not directly influence the neutrally stratified BBL.

As in Posada-Bedoya *et al.* (2024) and Posada-Bedoya *et al.* (2025*b*), the simulations were conducted with the pseudospectral code SPINS (Subich *et al.* 2013). The computational domain consisted of a 3-D channel with periodic boundary conditions

https://doi.org/10.1017/jfm.2026.12196 Published online by Cambridge University Press

in the streamwise (x) and spanwise (y) directions. The top and bottom boundary conditions were no-slip and no-flux. The channel had a length $L = 3L_w$, a width B and a constant depth H. A Chebyshev grid was employed in the vertical direction with grid points clustered near the top and bottom walls. A uniform grid was used in the horizontal directions. In case I, the initial condition was specified by extrapolating the 2-D simulation by Posada-Bedoya *et al.* (2024) to three dimensions after the passage of two ISWs, well before the instability began deforming the near-bed laminar vortex sheets. This was done to save computational time during the early laminar, 2-D flow stages, as in Fringer & Street (2003). Case II was initialised with the 2-D Dubreil–Jacotin–Long solution for the density and velocity fields. In both cases, a 1 % white-noise velocity perturbation was added to induce the growth of the 3-D instabilities.

Numerical parameters of the simulated cases are summarised in table 1, along with those from other studies in the literature. Case I can be considered a fully resolved direct numerical simulation, with $N(z^+ < 9) = 16$ (i.e. 16 grid points within the buffer sublayer at its thinnest point beneath the ISW). For case II, the resolution was $N(z^+ < 9) = 7$, which does not fully resolve the turbulent spectrum. The horizontal resolution (Δx, Δy) was ∼20 wall units. In comparison, the large eddy simulation (LES) by Sakai *et al.* (2020*a*) used 8 and 4 wall units in the streamwise and spanwise directions, respectively, together with 27 grid points within the buffer sublayer (table 1). Although the resolution in case II was insufficient to fully resolve the turbulent kinetic energy (TKE) budget across the full range of turbulent scales, it captures the dominant coherent structures governing transition in both laminar and turbulent upstream environments. Accordingly, our emphasis is on identifying the mechanisms governing transition to turbulence through analysis of the flow fields and coherent structures. Both simulations were run until the flow attained a statistically stationary state in the wave reference frame, with a turbulent wake extending across the entire domain.

3.3. *Flow analysis*

Coherent flow structures were identified through 2-D and 3-D visualisations of the velocity fluctuations ($\boldsymbol{u}_{3\text{-D}}$, see (3.10)) together with the instantaneous Q-criterion (Jeong & Hussain 1995). These diagnostics reveal coherent structures associated with both the modal instability and the bypass transition (e.g. Brinkerhoff & Yaras 2015; Bose & Durbin 2016). Here,

$$Q = \frac{1}{2}(\lambda_1^2 + \lambda_2^2 + \lambda_3^2) \tag{3.7}$$

represents the local balance between vorticity and shear strain, where λ_i are the eigenvalues of the velocity gradient $A_{ij} = \partial u_i/\partial x_j$. Positive values of Q identify regions where local rotation dominates strain, whereas negative values indicate strain-dominated regions.

To isolate the 3-D motion governing transition, we decomposed the instantaneous velocity field $\boldsymbol{u} = (u, v, w)$ into a 2-D slowly varying spanwise-averaged background flow in the (x, z) plane, defined in the frame of reference of the ISW ($u_{2\text{-D}}$, $w_{2\text{-D}}$) and the 3-D fluctuations ($\boldsymbol{u}_{3\text{-D}}$) following Caulfield & Peltier (2000) and Castro-Folker & Stastna (2024):

$$u(x, y, z, t) = u_{3\text{-D}}(x, y, z, t) + u_{2\text{-D}}(x, z, t), \tag{3.8}$$

$$w(x, y, z, t) = w_{3\text{-D}}(x, y, z, t) + w_{2\text{-D}}(x, z, t), \tag{3.9}$$

$$v(x, y, z, t) = v_{3\text{-D}}(x, y, z, t). \tag{3.10}$$

The 2-D base flow ($u_{2\text{-D}}$, $w_{2\text{-D}}$) was computed by spanwise averaging the low-pass-filtered instantaneous velocity field in the streamwise direction in the ISW frame of

https://doi.org/10.1017/jfm.2026.12196 Published online by Cambridge University Press

reference, with $L_w/2$ as the cutoff length scale. This filter scale is on the order of the distance over which the reverse-flow jet region develops after flow separation, producing a smoothly varying 2-D base flow.

Following the decomposition, turbulence intensity (Tu) and turbulent kinetic energy ($KE_{3\text{-D}}$) were used to quantity the strength of the 3-D fluctuations:

$$Tu = \frac{\sqrt{\left(u_{3\text{-D}}^2 + v_{3\text{-D}}^2 + w_{3\text{-D}}^2\right)/3}}{U_2}, \qquad KE_{3\text{-D}} = \frac{1}{2}\left(u_{3\text{-D}}^2 + v_{3\text{-D}}^2 + w_{3\text{-D}}^2\right). \tag{3.11}$$

We followed the nomenclature of Castro-Folker & Stastna (2024), using $\langle\cdot\rangle_p$ to denote averaging of a field $\cdot$ along dimension p in the ISW frame of reference. For example, $\langle Tu\rangle_{yt}$ denotes the time-averaged spanwise average of the turbulence intensity, yielding an (x, z)-dependent field.

Streaks (Klebanoff modes, Klebanoff (1971)) within the FST were characterised following Asai *et al.* (2007) and Brinkerhoff & Yaras (2015) using their mean energy ($\bar{u}_{streak}^2$) and spacing (Δy_{streak}). The mean and standard deviation of the streak energy were computed from time series of the maximum $u_{3\text{-D}}$ in successive $y-z$ planes at regularly spaced streamwise locations. The spanwise spacing was determined from the mean peak-to-peak distance between adjacent streaks in each $y-z$ plane.

The dominant flow scales associated with each transition pathway were quantified at selected representative times using the spanwise-averaged wavelet spectrum of the instantaneous streamwise velocity. The analysis was performed at the near-bed plane $z = \delta^*$, where δ^* denotes the boundary-layer displacement thickness.

4. Results

4.1. *Overview of the transition pathways*

Two distinct pathways to turbulence were identified beneath ISWs: a modal-instability pathway in initially laminar environments and a bypass pathway induced by FST.

At the laboratory scale, the transition to turbulence initially occurs through the growth of a laminar modal instability that generates packets of spanwise-oriented vortices in the wave wake (figure 2*c*, $t/T = 3.5$). Their breakdown produces localised turbulent patches that are advected and amplified by successive waves, which trigger further instabilities (figure 2*c*, $t/T = 5.5$), leading to a gradual increase in the boundary-layer-integrated TKE (figure 2*a*). After approximately six wave periods, turbulence occupies the entire domain, and the flow approaches a statistically stationary state (figure 2*c*, $t/T = 8$). In this regime, turbulence production is sustained by a bypass-transition mechanism triggered by FST upstream of the ISW. This mechanism is characterised by the appearance of elongated near-bed streaks of streamwise velocity fluctuations.

At the lake scale, the higher Reynolds number promotes rapid growth of the modal instability, resulting in continuous vortex shedding and a turbulent wake in the lee of the wave (figure 2*d*, $t/T = 0.3$). As the wave encounters turbulence generated during previous cycles, a bypass transition develops beneath the wave trough while modal-instability-driven turbulence persists downstream. The coexistence of modal and bypass transition produces a peak in the integrated TKE at $t/T \approx 0.88$ (figure 2*b*). As the bypass-generated turbulence propagates downstream, it suppresses the modal instability. The flow then evolves toward a statistically stationary state in which bypass transition becomes the dominant turbulence-generation mechanism (figure 2*d*, $t/T = 1.3$). As in the laboratory-scale simulations, this regime is characterised by elongated near-bed streaks of streamwise velocity fluctuations.

https://doi.org/10.1017/jfm.2026.12196 Published online by Cambridge University Press

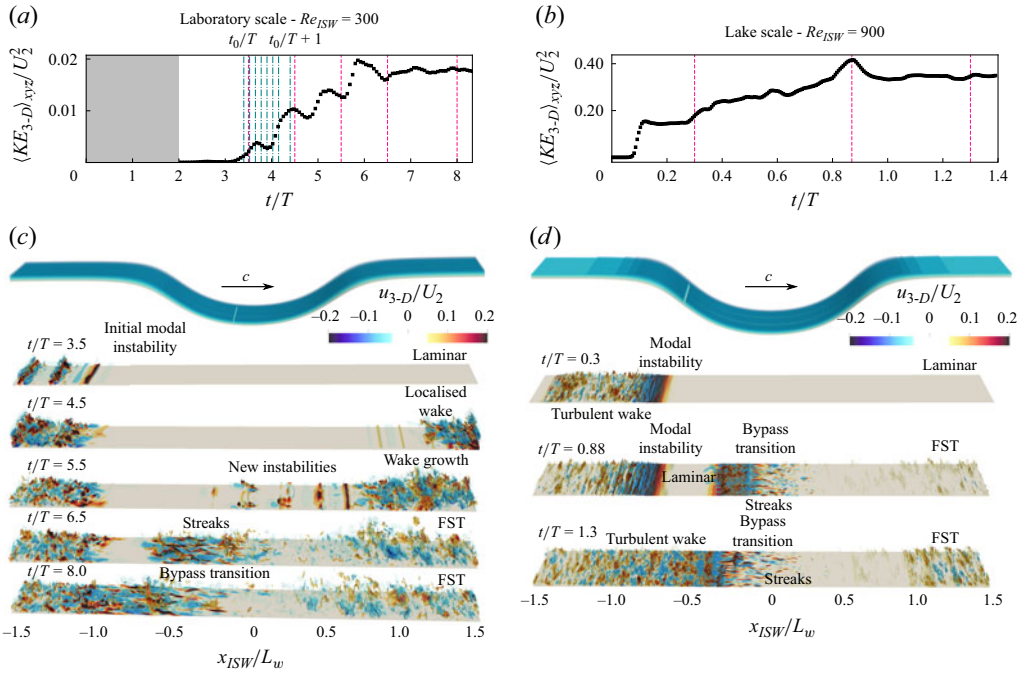


Figure 2. Time series of the near-bed averaged KE for (*a*) case I ($Re_{ISW} = 300$) and (*b*) case II ($Re_{ISW} = 900$). (c, d) Three-dimensional snapshots of near-bed streamwise velocity fluctuations $u_{3\text{-D}}$ (colour bar) and constant density surfaces (shades of blue) in the frame of reference of the ISW. The pink dashed lines in panels (*a*) and (*b*) indicate the times of the snapshots in panels (*c*) and (*d*), respectively. The dash-dotted lines indicate the times of the snapshots shown in figure 3. In panel (*a*), the grey shaded area indicates the initial two wave periods simulated in 2-D. Time is given in wave periods through the domain $T = 3L_w/c$. Animations of these simulations are presented in movies S1 ($Re_{ISW} = 300$) and S2 ($Re_{ISW} = 900$).

In the following sections, we examine how FST modifies the transition dynamics at each Re_{ISW}. To this end, we will focus on four instances of the simulations that provide conditions representative of laminar and bypass transition at laboratory and lake scales. For the bypass-transition cases, the analysis is restricted to the statistically stationary regime, in which the turbulent wake spans the entire domain and the turbulence statistics are near-steady in the wave reference frame.

4.2. *Laboratory scale ($Re_{ISW} = 300$)*

4.2.1. *Laminar-to-turbulent transition*

In an initially laminar background, the ISW-driven instability is convective and generates regularly spaced clusters of spanwise-oriented vortices in the wake of the ISW. These vortices break down into turbulent bursts via elliptical instability (figures 2 and 3).

The flow remained nearly 2-D during the first wave period, with negligible near-bed 3-D energy until $t/T \approx 3$ (figure 2*a*). Following the passage of the fourth wave, the instability amplified into packets of nearly 2-D, regularly spaced, spanwise-oriented vortices (figure 3, $t = t_0$). The streamwise separation of these vortices matched the wavelength of the most unstable mode predicted by linear stability theory (Posada-Bedoya *et al.* 2024). This mode is evident as a localised peak of wavelet power in the lee of the wave (figures 4*a* and 4b).

https://doi.org/10.1017/jfm.2026.12196 Published online by Cambridge University Press

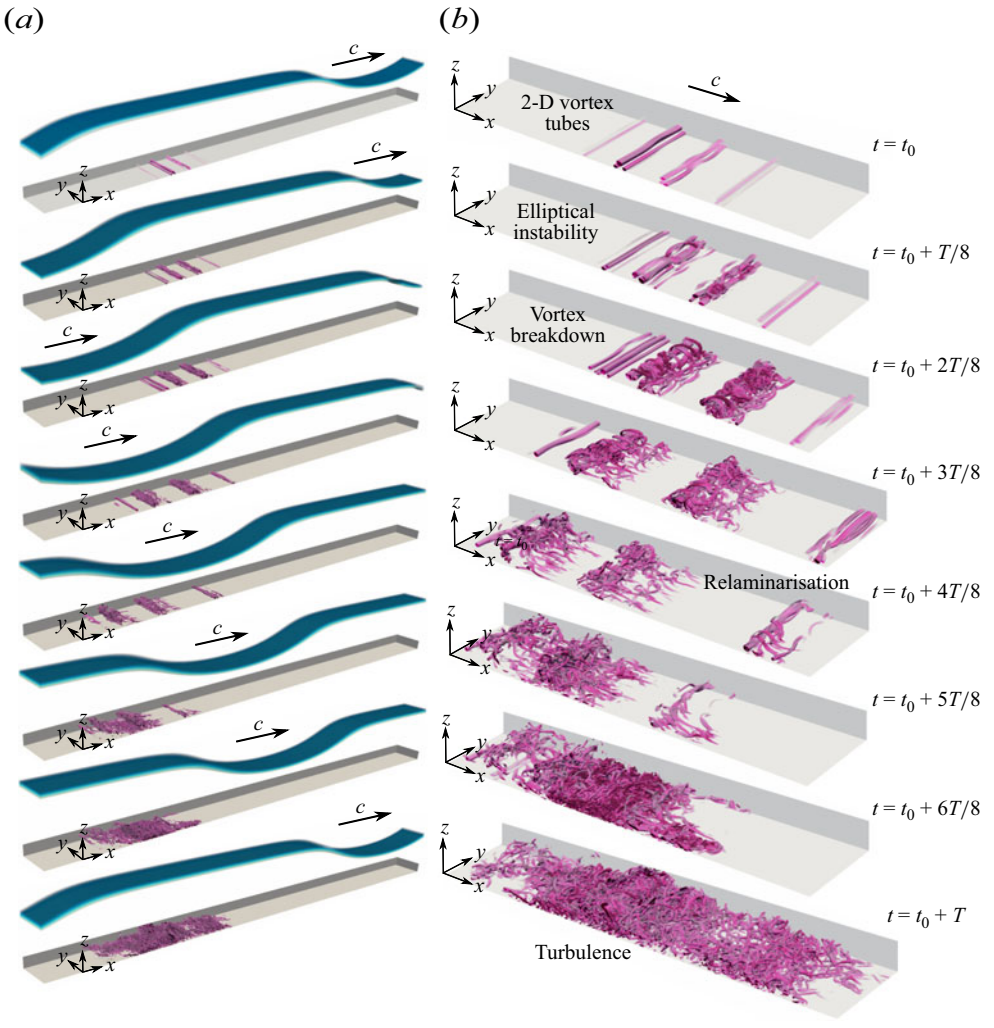


Figure 3. Flow field structure for case I ($Re_{ISW} = 300$) at selected times during a wave period over the entire domain. (*a*) Three-dimensional snapshots of constant density surfaces (shades of blue) and near-bed Q-criterion (shades of magenta). (*b*) Zoom-in of the Q-criterion in a fixed near-bed region of the panels on the left. The time of each snapshot is indicated for each row, where t_0 is a selected time after one wave period in the 3-D simulation. This simulation is also presented in movie S1.

As the vortices interact and are stretched by the background shear, they undergo spanwise elliptical instability (figure 3, $t = t_0 + T/8$) (Kerswell 2002; Leweke *et al.* 2016). This instability bends the vortex cores along their axes, consistent with the simulations by Sakai *et al.* (2020*a*) and canonical vortex-pair dynamics (Leweke & Williamson 1998). Continued deformation leads to secondary, smaller-scale instabilities within each vortex packet, resulting in breakdown into 3-D turbulence (figure 3, $t = t_0 + 2T/8$). The accompanying vortex breakdown produces a rapid increase in the near-bed integrated 3-D kinetic energy, which reaches a local maximum (figure 2*a*).

To verify that the domain width was sufficient to capture the dominant instability, we performed an additional simulation with a spanwise domain three times larger (Appendix A). No larger-scale modes emerged, confirming that the primary instability is fully resolved.

https://doi.org/10.1017/jfm.2026.12196 Published online by Cambridge University Press

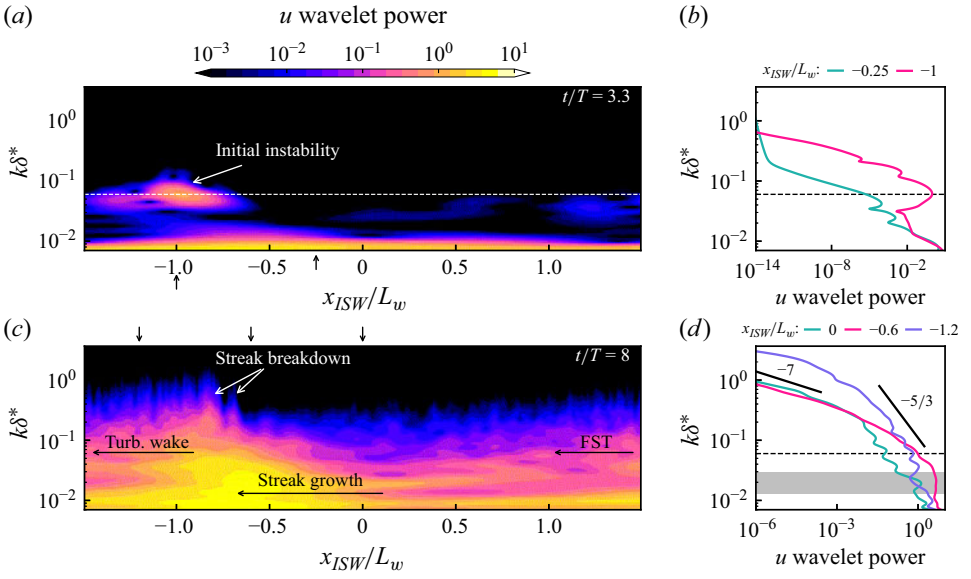


Figure 4. Spanwise-averaged wavelet spectrum of the instantaneous streamwise velocity evaluated at $z = \delta^*$ at (*a*,*b*) $t/T = 3.3$ and (*c*,*d*) $t/T = 8$ for case I ($Re_{ISW} = 300$). Here, $k\delta^*$ is the non-dimensional wavenumber. (*b*,*d*) Wavelet spectra at selected streamwise locations. The streamwise locations are indicated with black vertical arrows in panels (*a*) and (*c*). The horizontal dashed line in (*b*,*d*) indicates the wavenumber of the modal instability. The grey shade in d indicates the streamwise wavenumber band of the streaks.

Subsequent ISWs interact with residual vortices generated during previous wave passages. Beneath the front shoulder, the FPG stretches these structures in the streamwise direction, reducing the amplitude of the 3-D perturbations (figure 3, $t = t_0 + 3T/8$, $t = t_0 + 4T/8$). This is accompanied by a decrease in near-bed TKE(figure 2*a*), analogous to relaminarisation under strong acceleration (Narasimha & Sreenivasan 1979; Posada-Bedoya *et al.* 2024). Here, 'relaminarization' refers to the attenuation of the BBL instability and turbulent fluctuations, without the flow necessarily returning to a fully laminar state (Piomelli & Yuan 2013).

The weakened vortices induce finite-amplitude disturbances to the BBL that seed new instabilities in the lee of the wave (figure 3, from $t = t_0 + 5T/8$). The disturbances are subsequently reamplified, increasing both the extent and intensity of the turbulent wake (figure 2*a*). This cycle of partial relaminarisation followed by amplification is repeated with each wave passage, resulting in a gradual buildup of turbulent energy. This dynamics is consistent with the noise-amplifier behaviour identified in 2-D simulations (Posada-Bedoya *et al.* 2024). After ≈6.5 wave periods, the turbulent wake spans the entire near-bed region (figure 5) (see movie S1), and the integrated turbulent energy approaches a quasi-steady state (figure 2*a*).

Having established the modal transition pathway in the initially laminar environment, we next examine how persistent FST after ≈6.5 wave periods fundamentally alters the transition mechanism.

4.2.2. *Transition in the presence of a turbulent wake*

After ≈6.5 wave periods, the persistent FST upstream of the ISW fundamentally changes the transition mechanism. Instead of convective instability, the flow undergoes bypass transition. At this stage, both the background 2-D flow ($u_{2\text{-D}}$, figure 5(*a*)) and the

https://doi.org/10.1017/jfm.2026.12196 Published online by Cambridge University Press

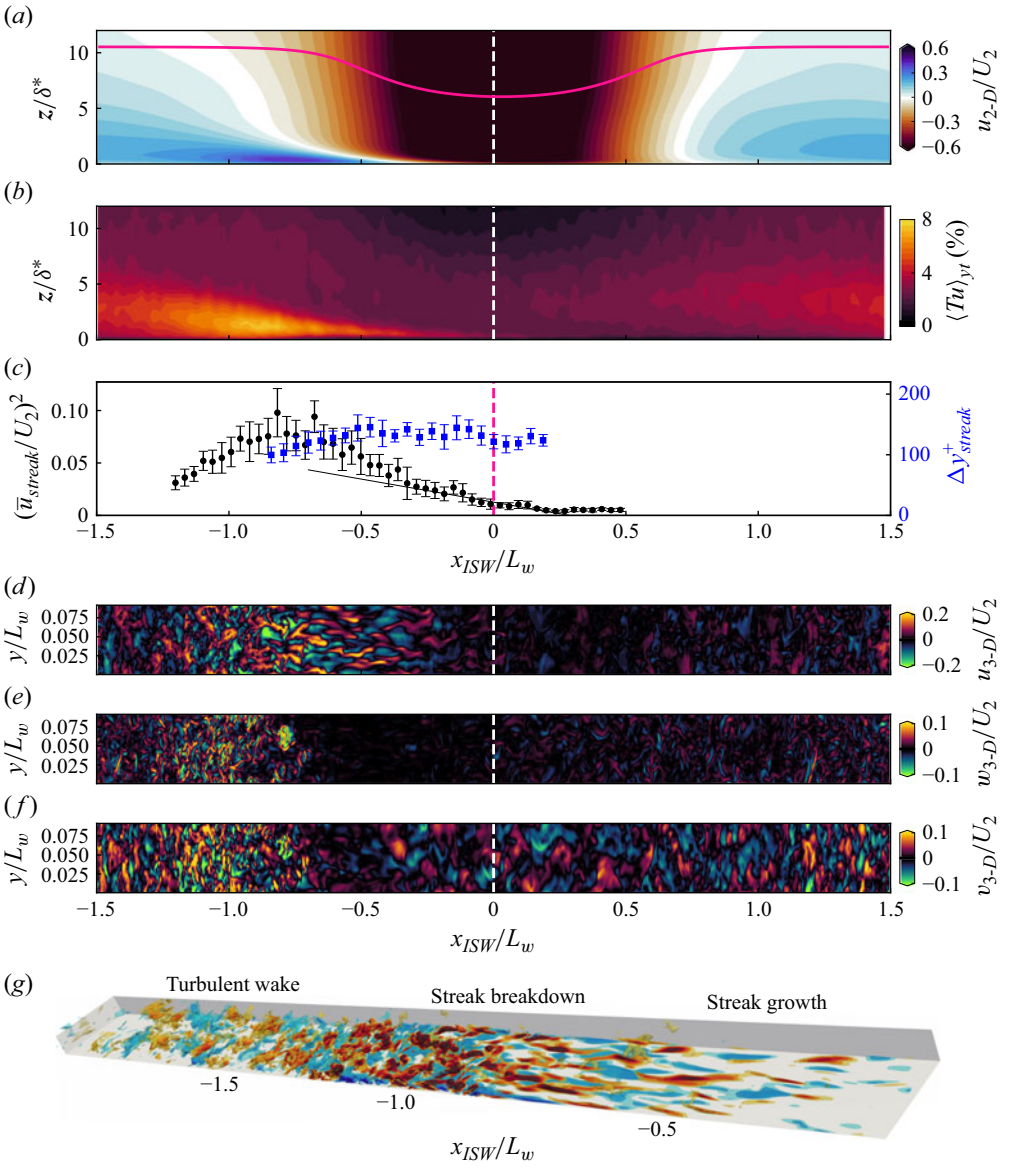


Figure 5. Velocity field and turbulence intensity for case I ($Re_{ISW} = 300$). Spanwise-averaged, (*a*) low-pass-filtered horizontal velocity $u_{2\text{-D}}$ and (*b*) turbulence intensity, time-averaged after $t/T \approx 6.5$ in the ISW frame of reference (x_{ISW}). (*c*) Streamwise variability of the average streak energy ($(\bar{u}_{streak}/U_2)^2$) and spacing (Δy^+_{streak}) after $t/T \approx 6.5$. Error bars indicate one standard deviation. Contours of the instantaneous (*d*) streamwise, (*e*) vertical and (*f*) spanwise velocity fluctuations at $z = \delta^*$ at a time $t/T = 8$, representative of the final nearly steady state. (*g*) Three-dimensional zoom-in of selected $u_{3\text{-D}}$ contours at $t/T = 8$. The pink line in a indicates the pycnocline depth, with H scaled to the y-axis extent. The vertical dashed line indicates the location of the ISW trough in panels (*a–f*).

turbulence intensity (Tu, figure 5(*b*)) are approximately steady. The near-bed (below $z/H = 0.15$) vertically averaged turbulence intensity at the leading edge of the ISW ($x_{ISW}/L_w = 1$) is $Tu \approx 3$ %, which we take as the representative upstream disturbance

https://doi.org/10.1017/jfm.2026.12196 Published online by Cambridge University Press

level. The FST is characterised by a broadband wavelet power whose intensity gradually decays downstream (figure 4*c*).

The turbulence intensity decreases beneath most of the front shoulder, but begins to increase downstream of $x_{ISW}/L_w \approx 0.1$ (figure 5*b*). This near-bed amplification of Tu is associated with the growth of streamwise streaks (Klebanoff modes), generated by FST through shear sheltering (Durbin & Wu 2007; Zaki 2013). These streaks are visible in the $u_{3\text{-D}}$ field over $-0.8 < x_{ISW}/L_w < 0$ (figure 5*d–g*), whereas the spanwise and vertical velocity fluctuations remain comparatively weak. The spectral signature of the streaks is the downstream increase in streamwise low-wavenumber wavelet power ($k\delta^* \approx 2 \times 10^{-2}$) between $x_{ISW}/L_w \approx 0$ and $x_{ISW}/L_w \approx -0.6$ (figures 4*c* and 4*d*).

The streak energy $(\bar{u}_{streak}/U_2)^2$ initially increases approximately linearly from its inception point (figure 5*c*), consistent with algebraic growth via the lift-up mechanism. The growth rate is well approximated by $(\bar{u}_{streak}/U_2)^2 = A(xU_2/\nu)$, with $A = 3 \times 10^{-6}$, in agreement with previous studies at similar turbulence levels (Asai *et al.* 2007; Brinkerhoff & Yaras 2015). The spanwise spacing of the streaks decreases from $\Delta y^+_{streak} \approx 150$ near inception to $\Delta y^+_{streak} \approx 100$ at breakdown ($x_{ISW}/L_w \sim -0.85$), consistent with that reported by Brinkerhoff & Yaras (2015).

As the streaks amplify within the separated BBL, they develop inflectional profiles and undergo secondary instability. Individual streaks then break down into 3D structures, generating localised turbulent bursts. These bursts merge to form a persistent turbulent wake, with peak intensity at $x_{ISW}/L_w \approx -0.85$ (figure 5*b*). The spectral signature of the streak breakdown is an increase in high-wavenumber wavelet power near $x_{ISW}/L_w \approx -0.7$. Downstream of the breakdown, the spectrum of the turbulent wake follows a $-5/3$ slope (figure 4*d*) ($x_{ISW}/L_w \approx -1.2$). At this stage, the spectral peak of the modal instability is no longer evident throughout the domain (cf. panels (*b*) and (*d*) in figure 4).

In this quasi-steady regime, the volume-integrated turbulence production associated with streak breakdown balances the volume-integrated viscous dissipation over the near-bed region. This bypass mechanism is fundamentally different from the convective modal instability observed under laminar conditions, providing a distinct pathway to turbulence in the presence of free-stream disturbances.

4.3. *Lake scale ($Re_{ISW} = 900$)*

4.3.1. *Laminar-to-turbulent transition*

At the lake scale, transition in an initially laminar environment is governed by modal instability, producing continuous quasi-2-D vortex shedding from the separated boundary layer. After adjustment from the initial condition, the background flow exhibits strong shear within the separated BBL (figure 6*a*). The resulting inflectional velocity profile supports a shear instability that emerges within the reverse-flow region. This instability is evident as quasi-2-D oscillations in the velocity fluctuations around $x_{ISW}/L_w \approx -0.6$ (figure 6*d–f*). As the vortices amplify, they develop secondary instabilities that manifest as spanwise undulations along their axes (figure 6*g*). These perturbations increase the spanwise velocity fluctuations (figure 6*e*) and evolve into Λ vortices whose crests lift away from the wall and break down into turbulence.

The turbulence intensity increases rapidly near the bed within the reverse-flow region, beginning at $x_{ISW}/L_w \approx -0.6$ (figure 6*b*). At $z = \delta^*$, Tu grows exponentially with downstream distance, consistent with modal instability, reaching $Tu \approx 12\%$ near $x_{ISW}/L_w \sim -0.72$, where the vortex breakdown begins (figure 6*c*). The resulting turbulence spreads away from the wall and forms a wake with nearly uniform intensity across the BBL. Downstream of the breakdown location, the turbulence decays

https://doi.org/10.1017/jfm.2026.12196 Published online by Cambridge University Press

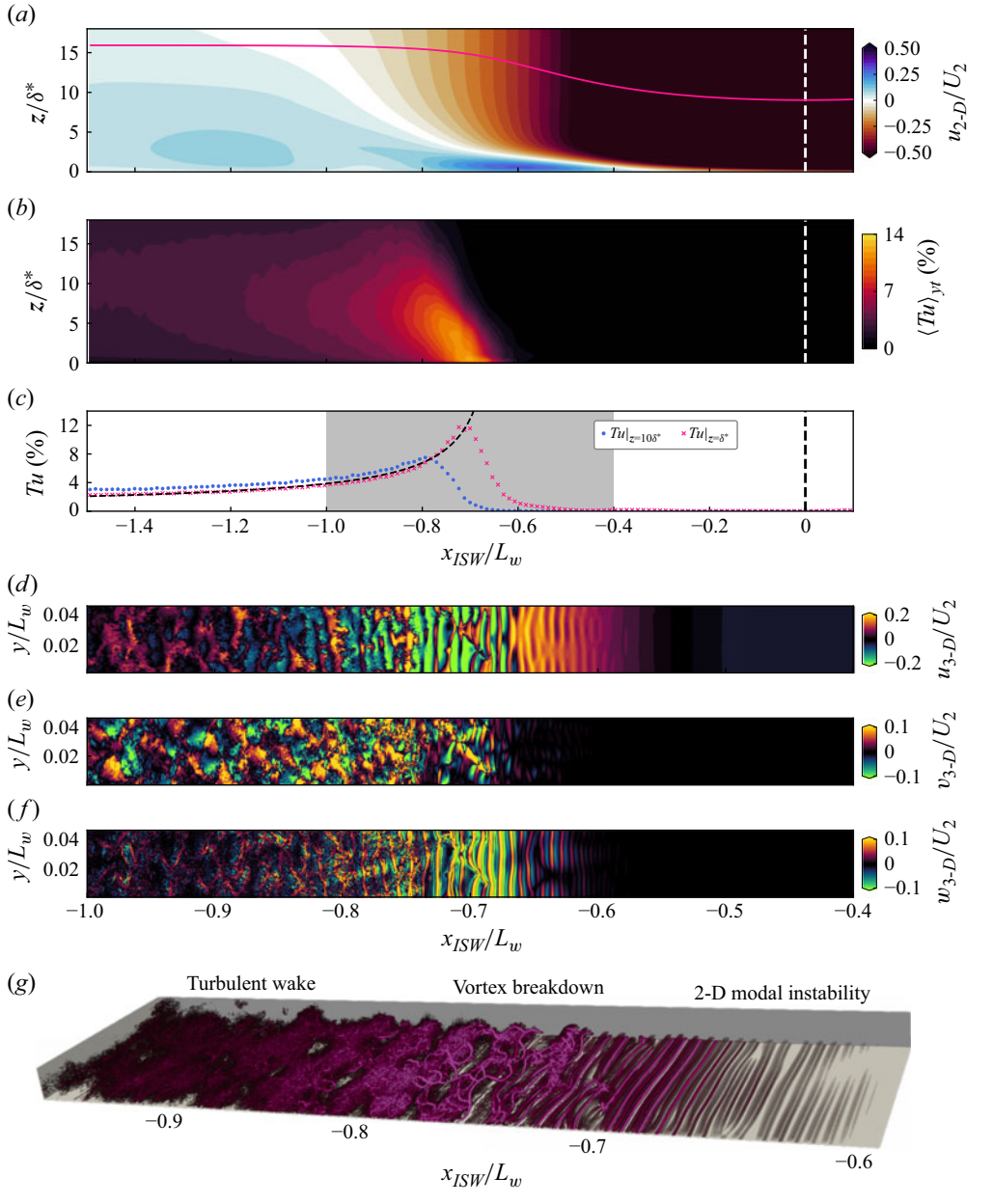


Figure 6. Flow field for case II ($Re_{ISW} = 900$) at $t/T = 0.59$, characteristic of $t/T < 1$. Spanwise-averaged, (*a*) low-pass-filtered horizontal velocity $u_{2\text{-}D}$ and (*b*) turbulence intensity, time-averaged during $0.3 < t/T < 0.7$ in the ISW frame of reference (x_{ISW}). (*c*) Transects of $\langle Tu \rangle_{yt}$ at $z = \delta^*$ and $z = 10\delta^*$, where δ^* is the boundary-layer displacement thickness at the ISW trough. The black dashed line in panel (*c*) indicates the $Tu \sim x^{-5/7}$ decay as in grid turbulence (Roach 1987). The grey shade in panel (*c*) indicates the region depicted in (*d–f*). Contours of the instantaneous (*d*) streamwise, (*e*) spanwise and (*f*) vertical velocity fluctuations at $z = \delta^*$ at a time $t/T = 0.59$. (*g*) Three-dimensional zoom-in of selected Q-criterion contours at $t/T = 0.59$, for $Q > 10$. The vertical dashed line in (*a–c*) indicates the location of the ISW trough. The pink line in panel (*a*) indicates the pycnocline depth, with H scaled to the y-axis extent. This simulation is also presented in movies S2 and S3.

https://doi.org/10.1017/jfm.2026.12196 Published online by Cambridge University Press

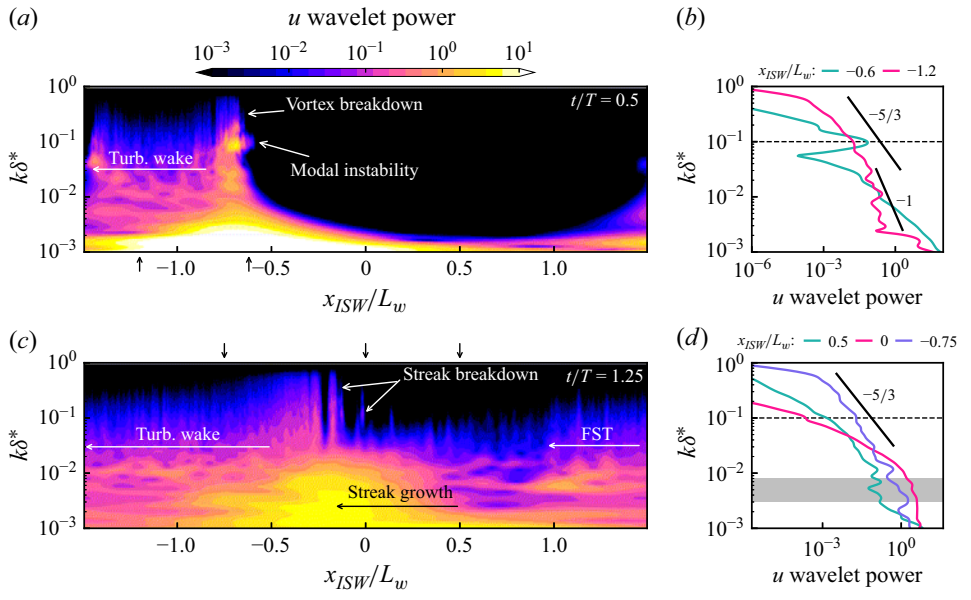


Figure 7. Spanwise-averaged wavelet spectrum of the instantaneous streamwise velocity evaluated at $z = \delta^*$ at (*a*,*b*) $t/T = 0.5$ and (*c*,*d*) $t/T = 1.25$ for case II ($Re_{ISW} = 900$). Here, $k\delta^*$ is the non-dimensional wavenumber. (*b*,*d*) Wavelet spectra at selected streamwise locations. The streamwise locations are indicated with black vertical arrows in panels (*a*,*c*). The horizontal dashed line in (*b*,*d*) indicates the wavenumber of the modal instability. The grey shade in (*d*) indicates the streamwise wavenumber band of the streaks.

approximately as $Tu \sim x^{-5/7}$, consistent with decaying grid turbulence (Roach 1987; Brinkerhoff & Yaras 2015).

Wavelet analysis confirms that the instability corresponds to the most unstable mode of the shear flow (Posada-Bedoya *et al.* 2024), with a peak for $k\delta^* \sim 10^{-1}$ at $x_{ISW}/L_w \approx -0.6$ (figures 7*a* and 7*b*). Vortex breakdown broadens the spectrum, indicating redistribution of energy across scales. Downstream, the turbulent wake exhibits a limited inertial range following a $-5/3$ scaling (figure 7*b*). At lower wavenumbers, the spectrum follows a shallower slope, closer to -1, as reported by Sakai *et al.* (2020*a*).

The inertial subrange is truncated at $k\delta^* \sim 10^0$ by the horizontal grid resolution (figure 7*b*), which is approximately 10 times smaller than the most unstable mode. The rapid decay at high wavenumbers reflects the combined effects of finite resolution and the second-order exponential spectral filter, rather than a fully resolved dissipation range. This demonstrates that our simulations resolve the dominant modal instability and its breakdown into smaller-scale structures, but not the complete turbulent cascade to the Kolmogorov scale. Having established the modal transition pathway in the absence of upstream disturbances, we next examine how persistent FST fundamentally alters the transition mechanism.

4.3.2. *Transition in the presence of a vortex wake*

After one wave period, the ISW propagates into the decaying vortex wake generated by modal instability during the passage of the preceding wave. The upstream turbulence intensity is $Tu \approx 1.8$ %. As in the laboratory-scale case, this residual turbulence triggers bypass transition. Unlike the laboratory-scale case, however, the stronger background shear

https://doi.org/10.1017/jfm.2026.12196 Published online by Cambridge University Press

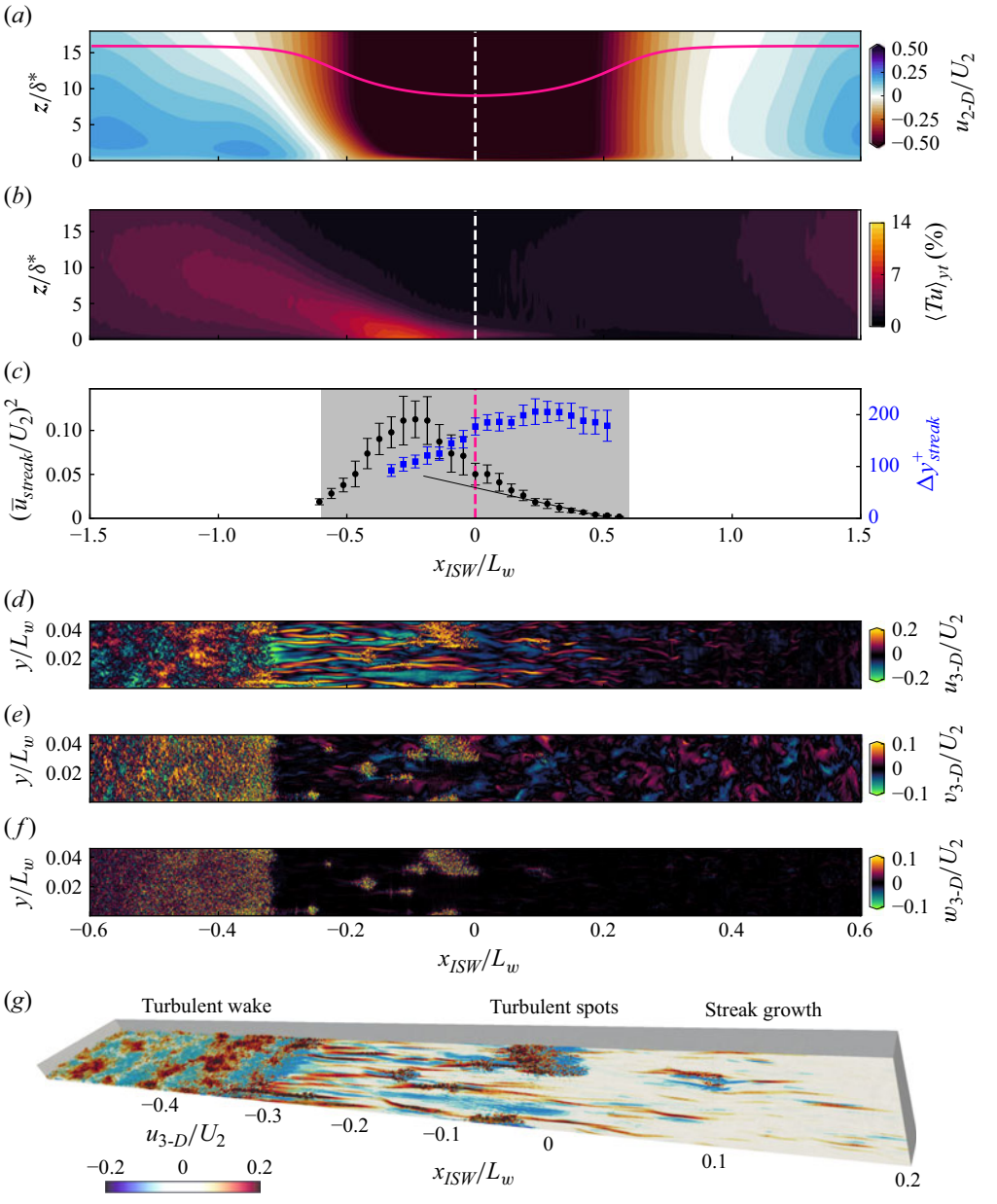


Figure 8. Flow field for case II ($Re_{ISW} = 900$) during $t/T > 1$. Spanwise-averaged, (*a*) low-pass-filtered horizontal velocity $u_{2\text{-D}}$ and (*b*) turbulence intensity, time-averaged after $t/T \approx 1.1$ in the ISW frame of reference (x_{ISW}). (*c*) Streamwise variability of the average streak energy ($(\bar{u}_{streak}/U_2)^2$) and spacing (Δy^+_{streak}). Contours of the instantaneous (*d*) streamwise, (*e*) spanwise and (*f*) vertical velocity fluctuations at $z = \delta^*$ at a time $t/T = 1.4$. (*g*) Three-dimensional zoom-in of selected $u_{3\text{-D}}$ contours at $t/T = 1.25$. The vertical dashed line in (*a–c*) indicates the location of the ISW trough. The grey shade in (*c*) indicates the region depicted in (*d–f*). The pink line in panel (*a*) indicates the pycnocline depth, with H scaled to the y-axis extent. This simulation is also presented in movies S2 and S3.

https://doi.org/10.1017/jfm.2026.12196 Published online by Cambridge University Press

causes streaks to form much farther upstream, within the favourable pressure-gradient region ($x_{ISW}/L_w \approx 0.5$) (figure 8 and movie S2).

Individual high-speed streaks undergo secondary instability and break down into turbulent spots both upstream and downstream of the ISW trough. These resulting turbulent spots propagate, merge and ultimately form a nearly spanwise-uniform turbulent zone. As a result, the onset of turbulence shifts upstream to $x_{ISW}/L_w \simeq -0.32$, significantly closer to the trough than in the laminar case ($x_{ISW}/L_w \simeq -0.72$), allowing bypass transition to occur before the modal instability can develop.

Wavelet analysis confirms the spectral signature of streak growth, with low-streamwise-wavenumber power increasing downstream of $x_{ISW}/L_w \approx 0.5$ (figures 7*c* and 7*d*). Streak breakdown is identified in the localised peaks of high-wavenumber power near the ISW trough. Complete transition at $x_{ISW}/L_w \simeq -0.32$ coincides with spectral broadening and the emergence of a downstream turbulent wake exhibiting $-5/3$ spectral scaling (figures 7*c* and 7*d*). The earlier onset of streak breakdown suppresses the modal instability. This is reflected in the disappearance of the spectral peak associated with the modal instability throughout the domain (cf. panels (*a*) and (*c*) in figure 7).

The streak energy again exhibits the algebraic growth characteristic of the lift-up mechanism near the inception point ($x_{ISW}/L_w \approx 0.5$), initially increasing approximately linearly downstream (figure 8*c*), with growth rate $A = 2 \times 10^{-7}$. This contrasts with the exponential growth of modal instability under laminar conditions.

The spanwise streak spacing decreases from $\Delta y^+_{streaks} \approx 200$ near inception ($x_{ISW}/L_w \sim 0.5$) to $\Delta y^+_{streaks} \approx 100$ near breakdown ($x_{ISW}/L_w \approx -0.32$), consistent with the stabilising influence of the FPG upstream. As streaks move downstream, increasing shear enhances their susceptibility to secondary instability (e.g. Durbin & Wu 2007; Zaki 2013). The numerical resolution was sufficient to resolve the streaks, with ≈6–8 grid points per streak in the spanwise direction ($\Delta y^+_{streak} \approx 100$).

The bypass-driven turbulent wake redistributes momentum within the separated boundary layer, homogenising the near-wall velocity field, pushing the BBL separation point farther upstream and weakening the shear within the separated BBL (cf. figures 6(*a*) and 8(*a*)) (see movie S3). The weakened background shear is expected to reduce the growth rate of any residual modal instability, further favouring the bypass-transition pathway.

5. Discussion

We identified two distinct pathways governing the transition to turbulence beneath ISWs: a modal-instability pathway in initially laminar environments and a bypass pathway triggered by FST. These pathways, summarised schematically in figure 9, depend strongly on both Reynolds number and FST intensity. This provides a framework for interpreting both laboratory and field observations.

Our simulations demonstrate that FST fundamentally alters the transition dynamics beneath ISWs through a bypass-transition mechanism that supersedes the modal instability observed in initially laminar environments. This mechanism provides a unified explanation for several field observations reported by Quaresma *et al.* (2007) and Zulberti *et al.* (2020) that have remained difficult to reconcile with the modal-instability framework. Four consequences of bypass transition are particularly important: (i) streak amplification increases KE beneath the front shoulder of the wave; (ii) turbulence onset is farther upstream, closer to the ISW trough; (iii) turbulent momentum transport modifies the mean

https://doi.org/10.1017/jfm.2026.12196 Published online by Cambridge University Press

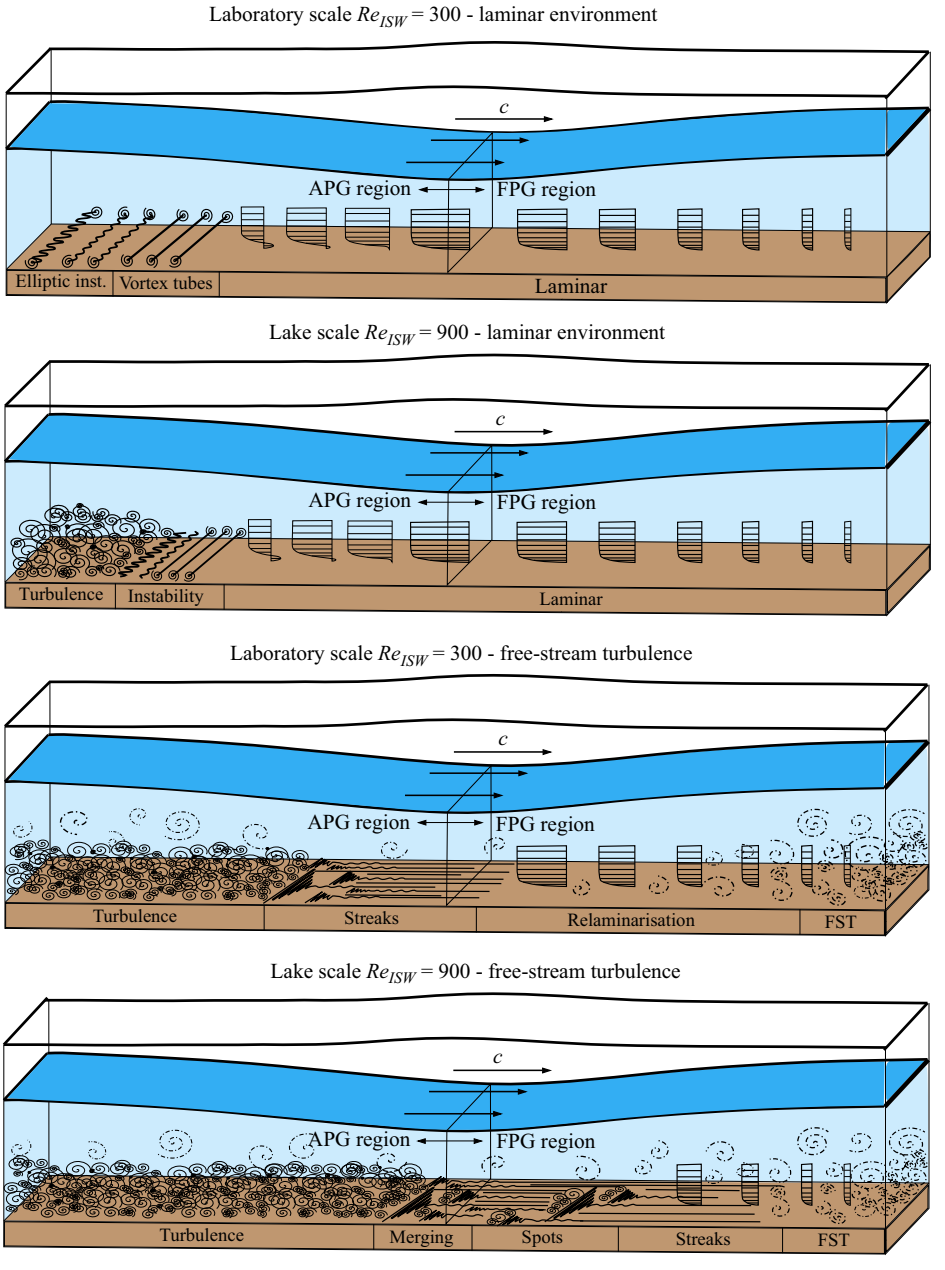


Figure 9. Conceptual sketch of the different pathways for the transition to turbulence depending on the Reynolds number and the antecedent FST. Based on a similar sketch by Önder & Liu (2020) for a surface solitary wave.

flow, weakening separation and flow reversal; and (iv) the modal instability is suppressed, eliminating its characteristic spectral signature.

The suppression of the modal-instability pathway is evidenced by the disappearance of its characteristic spectral peak once bypass transition becomes established (figures 4 and 7). This is consistent with the observations of Zulberti *et al.* (2020), who found no identifiable spectral signature associated with a shear instability. Rather, turbulence

https://doi.org/10.1017/jfm.2026.12196 Published online by Cambridge University Press

developed continuously beneath the front shoulder of the wave and reached a maximum shortly after trough passage. The simulations exhibit similar evolution, with KE increasing through the amplification and breakdown of streaks beneath the front shoulder (figure 7).

Bypass transition also substantially modifies the background flow. The bypass-generated turbulent wake redistributes momentum within the separated BBL, homogenising the near-wall velocity field and shifting the separation point downstream relative to the laminar case (movie S3). As a result, the recirculation region and associated flow reversal are significantly weakened. This behaviour is consistent with the absence of flow separation and reversal reported by Zulberti *et al.* (2020), suggesting that discrepancies between field observations and simulations assuming initially laminar conditions arise primarily from differences in the transition pathway. Whereas flow reversal is a defining feature of the modal-instability pathway, it can be substantially attenuated or even eliminated by enhanced near-bed momentum mixing from a sufficiently strong bypass transition.

The location of transition is controlled by both FST intensity and Reynolds number. As either parameter increases, streaks form and undergo breakdown progressively farther upstream, shifting turbulence production closer to the ISW trough. Extrapolation of this trend to field-scale conditions suggests that transition may occur directly beneath the trough, consistent with observations of peak turbulence and sediment concentration immediately following trough passage (e.g. Quaresma *et al.* 2007; Zulberti *et al.* 2020). This behaviour contrasts with the modal-instability pathway, in which turbulence develops farther downstream.

The shift in transition location has direct implications for sediment transport. Figure 10 shows the spatial distribution of the friction coefficient,

$$C_f = \frac{|\tau_b|}{\frac{1}{2}\rho_0 U_2^2}, \qquad \tau_b = \nu\rho_0\left(\frac{\partial u}{\partial z}\right)_{z=0}, \tag{5.1}$$

for both modal and bypass-transition regimes. In both transition regimes, the maximum bed stress coincides with the onset of turbulence, occurring substantially closer to the ISW trough during bypass transition (figure 10*c*). Interestingly, the modal transition exhibits a peak stress approximately twice as large as that of the bypass transition. The spatial distribution of the bed stress also reflects the underlying transition mechanism. Modal instability produces a predominantly 2-D, quasiperiodic pattern with little spanwise variability (figure 10*a*), whereas bypass transition generates localised stress bursts associated with streak breakdown and strong spanwise modulation induced by the streaks themselves (figure 10*b*).

This spanwise variability provides a potential mechanism for bedform initiation. Regions of enhanced and reduced stress may promote preferential sediment accumulation aligned with the streaks, which can subsequently be reworked by the vortical structures generated during streak breakdown. Similar mechanisms have been proposed for the initiation of bedforms in turbulent boundary layers (Folk 1976; Best 1992). These results suggest that the transition pathway influences not only the magnitude and location of sediment mobilisation, but also its spatial organisation and, potentially, the initiation of bedforms.

At both laboratory and lake scales, the laminar-transition pathways observed in the present 3-D simulations closely resemble those reported in the corresponding 2-D

https://doi.org/10.1017/jfm.2026.12196 Published online by Cambridge University Press

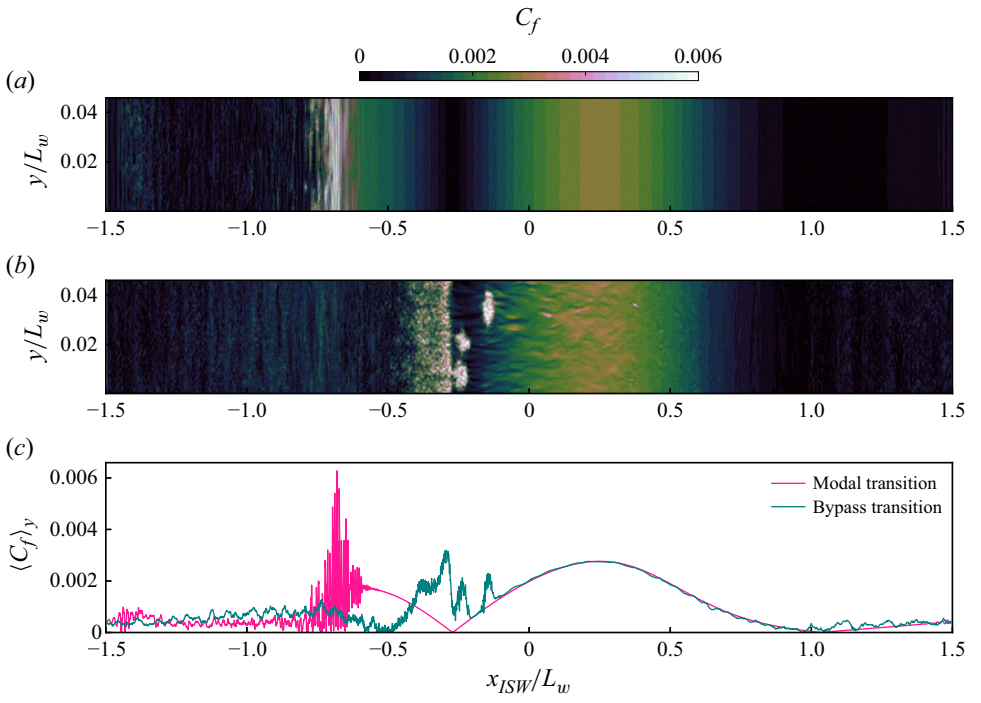


Figure 10. Spatial distribution of the friction coefficient C_f for case II ($Re_{ISW} = 900$) at (*a*) $t/T = 0.5$ (modal transition) and (*b*) $t/T = 1.25$ (bypass transition). (*c*) Spanwise-averaged C_f associated with panels (*a*) and (*b*).

simulations of Posada-Bedoya *et al.* (2024). Specifically, transition occurs through a convective modal instability at the laboratory scale and through sustained vortex shedding at the lake scale. This behaviour is consistent with previous studies of ISW propagation over initially laminar boundary layers (e.g. Stastna & Lamb 2002; Diamessis & Redekopp 2006; Stastna & Lamb 2008).

The laminar lake-scale results are particularly comparable to several field observations that show near-bed maxima in the sediment concentrations near the trailing edge of the wave (Johnson *et al.* 2001; Bogucki *et al.* 2005; Becherer *et al.* 2020; Trowbridge *et al.* 2025), likely driven by vortex shedding associated with the modal instability. Low near-bed sediment concentrations prior to ISW passage in those observations suggest initially laminar or weakly perturbed conditions, under which the modal-instability pathway is expected to dominate transition.

The laminar lake-scale results are also comparable to the LESs of Sakai *et al.* (2020*a*), who examined a laboratory-scale ISW propagating over a laminar opposing current. Their simulations exhibited a global oscillator that generated continuous vortex shedding, similar to the behaviour observed in our $Re_{ISW} = 900$ simulations for $t/T \lesssim 1$ (figure 6). A notable difference, however, is the absence, in our configuration, of the separation bubble and reattachment region commonly associated with globally unstable flows (e.g. Stastna & Lamb 2002; Diamessis & Redekopp 2006; Stastna & Lamb 2008) and reported in the ISW simulations of Sakai *et al.* (2020*a*).

While the laminar-transition dynamics is largely consistent with previous studies, the present 3-D simulations reveal a transition pathway that is inaccessible with 2-D models.

https://doi.org/10.1017/jfm.2026.12196 Published online by Cambridge University Press

In the presence of a turbulent wake, FST excites Klebanoff modes whose inherent 3-D structure leads to bypass transition. Interestingly, the 2-D simulations of Posada-Bedoya *et al.* (2024) nevertheless exhibited trends consistent with the influence of this mechanism, including an upstream shift in the onset of vortex-shedding and a reduction of the separated region with increasing wake intensity and Reynolds number. The present results suggest that these trends reflect the increasing importance of turbulence-induced momentum transport, which progressively weakens the separated shear layer and ultimately allows the bypass-transition pathway to supersede the modal instability pathway.

We note a limitation of the $Re_{ISW} = 900$ simulations related to numerical resolution. The model employs a second-order exponential spectral filter to control aliasing errors. Although the filter preserves sharp gradients, it can generate low-amplitude oscillations ('ringing') that persist over several grid points (Subich *et al.* 2013). In the present simulations, however, the strong near-bed shear rapidly attenuates high-wavenumber disturbances (Durbin & Wu 2007; Zaki 2013), thereby reducing the influence of any residual ringing on the transition dynamics. Any remaining ringing would be analogous to weak high-frequency free-stream disturbances. Such perturbations may modify the amplitude of the forcing experienced by the boundary layer, but they are unlikely to alter the bypass-transition mechanism identified here. Furthermore, the streaks governing bypass transition are resolved by approximately 6–8 grid points in the spanwise direction. Although the resolution does not capture the full turbulence spectrum to close the turbulence budget at the smallest scales, it is sufficient to resolve the coherent structures governing both the modal- and bypass-transition pathways. Consequently, the principal conclusions regarding the transition pathways are expected to be robust.

Despite this limitation, the $Re_{ISW} = 900$ simulations suggest that the downstream turbulent wakes exhibit similar behaviour following the two transition pathways. In particular, the resolved-scale turbulence spectra and the downstream decay of turbulence are qualitatively similar in the modal- and bypass-transition cases. This suggests that, although the mechanisms responsible for generating turbulence differ fundamentally beneath the wave, the resulting turbulent wake may progressively become less dependent on its transition history. Because the present resolution does not capture the full range of dissipative scales, however, differences in the small-scale dynamics, energy dissipation and KE budget cannot be quantified reliably. Fully resolved simulations would therefore be valuable for determining whether the apparent similarity in wake evolution persists across the full turbulence spectrum and for establishing whether the downstream wake can be described using parameterisations that are largely independent of the transition pathway.

To further bridge the gap between laboratory, lake and ocean-scale observations, future numerical studies should extend these simulations to higher Re_{ISW} and to FST intensities representative of oceanic conditions, for example driven by constant (e.g. Sakai *et al.* 2020*a*) and/or periodic (e.g. Posada-Bedoya *et al.* 2025*a*) background currents. Such simulations would enable systematic assessment of the role of FST intensity in the bypass-transition mechanism, the development of the turbulent wake downstream of the wave and the resulting sediment transport. Further complexity arises under realistic field conditions, where the BBL may be weakly stratified (e.g. Bogucki *et al.* 2005) and may coexist with a nepheloid layer (e.g. Zulberti *et al.* 2020); the influence of these features on BBL dynamics and sediment transport therefore warrants investigation in future process-oriented studies. Despite these open questions, the present results demonstrate that FST can fundamentally alter the pathway to turbulence beneath ISWs, providing a framework for reconciling observations across laboratory, numerical and field environments.

https://doi.org/10.1017/jfm.2026.12196 Published online by Cambridge University Press

6. Conclusions

We conducted high-resolution 3-D spectral numerical simulations to investigate the transition to turbulence beneath ISWs. We found that the transition pathway depends critically on both Reynolds number and the level of FST, providing a unified framework for interpreting the wide range of behaviours reported in laboratory, numerical and field studies.

In laminar environments, transition is governed by the modal-instability pathway at both laboratory and lake scales. At the laboratory scale, a convective modal instability produces discrete vortex clusters that break down via elliptical instability, generating localised turbulent bursts in the wave wake. At the lake scale, transition occurs through continuous amplification of the most unstable boundary-layer mode, resulting in sustained vortex shedding and turbulence downstream of the wave.

In contrast, when FST is present, the modal pathway can be bypassed. Environmental disturbances generate streamwise streaks (Klebanoff modes) beneath the front shoulder of the wave, which amplify and undergo secondary instability. The resulting turbulent spots merge to form a turbulent boundary layer closer to the ISW trough, precluding the development of the modal-instability pathway in the wake. This bypass mechanism, while well known in canonical boundary-layer transition, is newly identified here in the context of ISW-driven flows.

Under bypass transition, turbulence onset shifts upstream with increasing Reynolds number and FST intensity. This behaviour explains the variability in observed turbulence and sediment concentration patterns beneath ISWs, ranging from well-downstream peaks in laminar laboratory settings to near-trough maxima in highly turbulent field environments.

Overall, these findings demonstrate that ambient turbulence fundamentally alters the transition dynamics beneath ISWs. Accounting for FST is therefore essential for accurately predicting transition, near-bed turbulence, sediment transport and benthic boundary-layer dynamics in natural systems.

Supplementary movies. Supplementary movies are available at https://doi.org/10.1017/jfm.2026.12196.

Acknowledgements. The authors thank Peter Diamessis, Ugo Piomelli and Ryan Mulligan for comments on an earlier version of this manuscript. We thank the three anonymous reviewers for their valuable insights, which helped us improve the manuscript. This research made use of the high-performance computing clusters of Compute Ontario (computeontario.ca) and the Digital Research Alliance of Canada (alliancecan.ca). During the preparation of this manuscript, the authors used ChatGPT (OpenAI) to assist with language editing and phrasing. The tool was used only to improve clarity and readability.

Funding. The research was supported by two NSERC Discovery Grants to L.B. and J.O. and by Queen's University.

Declaration of interests. The authors report no conflict of interest.

Author contributions. J.O. and L.B.: supervision, writing – reviewing and editing. A.P.-B.: conceptualisation, numerical simulations, visualisation, writing – original draft preparation.

Data availability statement. Data are available from the authors upon request.

Appendix A. Sensitivity to spanwise length

Case IA considered the same set-up as case I over a domain three times wider (see table 1). Snapshots in figure 11 track the growth of the packets of vortex tubes, their elliptical instability in the spanwise direction and the beginning of vortex breakdown, very similar

https://doi.org/10.1017/jfm.2026.12196 Published online by Cambridge University Press

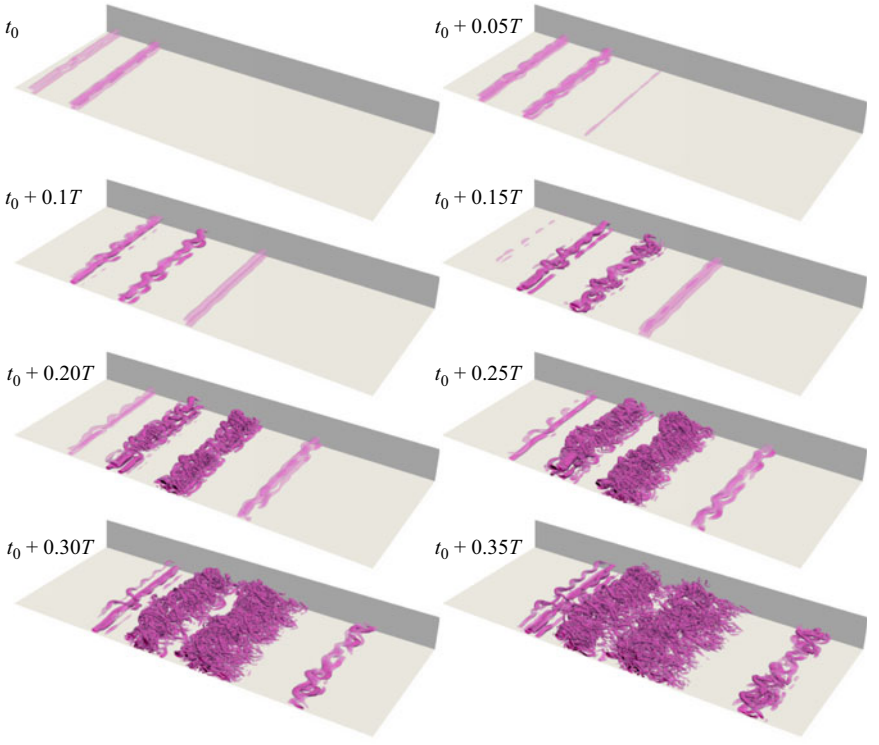


Figure 11. Three-dimensional snapshots of near-bed Q-criterion (shades of magenta) in a fixed near-bed region for simulation case IA, $Re_{ISW} = 300$. The time of each snapshot is indicated in the figure, where t_0 is a selected time after one wave period of the 3-D simulation.

to the one described (cf. figure 3). Importantly, no larger mode developed in the extended domain, which validates the 3-D transition path described for case I.

References

Aghsaee, P. & Boegman, L. 2015 Experimental investigation of sediment resuspension beneath internal solitary waves of depression. *J. Geophys. Res.: Oceans* **120** (5), 3301–3314.

Aghsaee, P., Boegman, L., Diamessis, P.J. & Lamb, K.G. 2012 Boundary-layer-separation-driven vortex shedding beneath internal solitary waves of depression. *J. Fluid Mech.* **690**, 321–344.

Alam, M. & Sandham, N.D. 2000 Direct numerical simulation of 'short' laminar separation bubbles with turbulent reattachment. *J. Fluid Mech.* **410**, 1–28.

Asai, M., Konishi, Y., Oizumi, Y. & Nishioka, M. 2007 Growth and breakdown of low-speed streaks leading to wall turbulence. *J. Fluid Mech.* **586**, 371–396.

Becherer, J., Moum, J.N., Colosi, J.A., Lerczak, J.A. & McSweeney, J.M. 2020 Turbulence asymmetries in bottom boundary layer velocity pulses associated with onshore-propagating nonlinear internal waves. *J. Phys. Oceanogr.* **50** (8), 2373–2391.

Best, J. 1992 On the entrainment of sediment and initiation of bed defects: insights from recent developments within turbulent boundary layer research. *Sedimentology* **39** (5), 797–811.

Boegman, L., Imberger, J., Ivey, G.N. & Antenucci, J.P. 2003 High-frequency internal waves in large stratified lakes. *Limnol. Oceanogr.* **48** (2), 895–919.

Boegman, L. & Stastna, M. 2019 Sediment resuspension and transport by internal solitary waves. *Annu. Rev. Fluid Mech.* **51** (1), 129–154.

Bogucki, D.J. & Redekopp, L.G. 1999 A mechanism for sediment resuspension by internal solitary waves. *Geophys. Res. Lett.* **26** (9), 1317–1320.

Bogucki, D.J., Redekopp, L.G. & Barth, J. 2005 Internal solitary waves in the coastal mixing and optics 1996 experiment: multimodal structure and resuspension. *J. Geophys. Res.: Oceans* **110**, C02024.

https://doi.org/10.1017/jfm.2026.12196 Published online by Cambridge University Press

BOSE, R. & DURBIN, P.A. 2016 Transition to turbulence by interaction of free-stream and discrete mode perturbations. *Phys. Fluids* **28** (11), 114105.
BOURGAULT, D., MORSILLI, M., RICHARDS, C., NEUMEIER, U. & KELLEY, D.E. 2014 Sediment resuspension and nepheloid layers induced by long internal solitary waves shoaling orthogonally on uniform slopes. *Cont. Shelf Res.* **72**, 21–33.
BRINKERHOFF, J.R. & YARAS, M.I. 2015 Numerical investigation of transition in a boundary layer subjected to favourable and adverse streamwise pressure gradients and elevated free stream turbulence. *J. Fluid Mech.* **781**, 52–86.
CARR, M., DAVIES, P.A. & SHIVARAM, P. 2008 Experimental evidence of internal solitary wave-induced global instability in shallow water benthic boundary layers. *Phys. Fluids* **20** (6), 066603.
CASTRO-FOLKER, N. & STASTNA, M. 2024 On the three-dimensional structure of instabilities beneath shallow-shoaling internal waves. *J. Fluid Mech.* **995**, R2.
CAULFIELD, C.-C.P. & PELTIER, W.R. 2000 The anatomy of the mixing transition in homogeneous and stratified free shear layers. *J. Fluid Mech.* **413**, 1–47.
DIAMESSIS, P.J. & REDEKOPP, L.G. 2006 Numerical investigation of solitary internal wave-induced global instability in shallow water benthic boundary layers. *J. Phys. Oceanogr.* **36** (5), 784–812.
DOROSTKAR, A., BOEGMAN, L. & POLLARD, A. 2017 Three-dimensional simulation of high-frequency nonlinear internal wave dynamics in cayuga lake. *J. Geophys. Res.: Oceans* **122** (3), 2183–2204.
DURBIN, P. & WU, X. 2007 Transition beneath vortical disturbances. *Annu. Rev. Fluid Mech.* **39**, 107–128.
FARMER, D. & ARMI, L. 1999 The generation and trapping of solitary waves over topography. *Science* **283** (5399), 188–190.
FARMER, D.M. 1978 Observations of long nonlinear internal waves in a lake. *J. Phys. Oceanogr.* **8** (1), 63–73.
FOLK, R.L. 1976 Rollers and ripples in sand, streams and sky: rhythmic alteration of transverse and longitudinal vortices in three orders. *Sedimentology* **23** (5), 649–668.
FRINGER, O.B. & STREET, R.L. 2003 The dynamics of breaking progressive interfacial waves. *J. Fluid Mech.* **494**, 319–353.
HELFRICH, K.R. & MELVILLE, W.K. 2006 Long nonlinear internal waves. *Annu. Rev. Fluid Mech.* **38**, 395–425.
HERBERT, T. 1988 Secondary instability of boundary layers. *Annu. Rev. Fluid Mech.* **20** (1), 487–526.
HUNT, J.C.R. & DURBIN, P.A. 1999 Perturbed vortical layers and shear sheltering. *Fluid Dyn. Res.* **24** (6), 375.
JEONG, J. & HUSSAIN, F. 1995 On the identification of a vortex. *J. Fluid Mech.* **285**, 69–94.
JOHNSON, D.R., WEIDEMANN, A. & PEGAU, W.S. 2001 Internal tidal bores and bottom nepheloid layers. *Cont. Shelf Res.* **21** (13–14), 1473–1484.
KERSWELL, R.R. 2002 Elliptical instability. *Annu. Rev. Fluid Mech.* **34** (1), 83–113.
KLEBANOFF, P.S. 1971 Effect of free-stream turbulence on a laminar boundary layer. *Bull. Am. Phys. Soc.* **10** (11), 1323.
KLEISER, L. & ZANG, T.A. 1991 Numerical simulation of transition in wall-bounded shear flows. *Annu. Rev. Fluid Mech.* **23**, 495–537.
LANDAHL, M.T. 1980 A note on an algebraic instability of inviscid parallel shear flows. *J. Fluid Mech.* **98** (2), 243–251.
LEWEKE, T., LE DIZÈS, S. & WILLIAMSON, C.H.K. 2016 Dynamics and instabilities of vortex pairs. *Annu. Rev. Fluid Mech.* **48** (1), 507–541.
LEWEKE, T. & WILLIAMSON, C.H.K. 1998 Cooperative elliptic instability of a vortex pair. *J. Fluid Mech.* **360**, 85–119.
NARASIMHA, R. & SREENIVASAN, K.R. 1979 Relaminarization of fluid flows. *Adv. Appl. Mech.* **19**, 221–309.
ÖNDER, A. & LIU, P.L.-F. 2020 Stability of the solitary wave boundary layer subject to finite-amplitude disturbances. *J. Fluid Mech.* **896**, A20.
PIOMELLI, U. & YUAN, J. 2013 Numerical simulations of spatially developing, accelerating boundary layers. *Phys. Fluids* **25** (10), 101304.
POSADA-BEDOYA, A., OLSTHOORN, J. & BOEGMAN, L. 2024 The boundary layer instability beneath internal solitary waves and its sensitivity to vortex wakes. *J. Fluid Mech.* **990**, A18.
POSADA-BEDOYA, A., OLSTHOORN, J. & BOEGMAN, L. 2025*a* Bedform growth bene*a*th periodic internal solitary waves propagating through a tidal flow. *J. Geophys. Res.: Oceans* **130** (8), e2025JC022914.
POSADA-BEDOYA, A., OLSTHOORN, J. & BOEGMAN, L. 2025*b* Roughness-induced *b*oundary-layer instability beneath internal solitary waves. *J. Fluid Mech.* **1009**, A21.
QUARESMA, L.S., VITORINO, J., OLIVEIRA, A. & DA SILVA, J. 2007 Evidence of sediment resuspension by nonlinear internal waves on the western Portuguese mid-shelf. *Mar. Geol.* **246** (2–4), 123–143.

https://doi.org/10.1017/jfm.2026.12196 Published online by Cambridge University Press

ROACH, P.E. 1987 The generation of nearly isotropic turbulence by means of grids. *Intl J. Heat Fluid Flow* **8** (2), 82–92.

SAKAI, T., DIAMESSIS, P.J. & JACOBS, G.B. 2020*a* Self-sustained instability, transition, and turbulence induced by a long separation bubble in the footprint of an internal solitary wave. I. Flow topology. *Phys. Rev. Fluids* **5** (10), 103801.

SAKAI, T., DIAMESSIS, P.J. & JACOBS, G.B. 2020*b* Self-sustained instability, transition, and turbulence induced by a long separation bubble in the footprint of an internal solitary wave. II. Flow statistics. *Phys. Rev. Fluids* **5** (10), 103802.

SPALART, P.R. & STRELETS, M.K. 2000 Mechanisms of transition and heat transfer in a separation bubble. *J. Fluid Mech.* **403**, 329–349.

STASTNA, M. & LAMB, K.G. 2002 Vortex shedding and sediment resuspension associated with the interaction of an internal solitary wave and the bottom boundary layer. *Geophys. Res. Lett.* **29** (11), 1512.

STASTNA, M. & LAMB, K.G. 2008 Sediment resuspension mechanisms associated with internal waves in coastal waters. *J. Geophys. Res.* **113** (C10), C10016.

SUBICH, C.J., LAMB, K.G. & STASTNA, M. 2013 Simulation of the Navier–Stokes equations in three dimensions with a spectral collocation method. *Intl J. Numer. Methods Flow* **73** (2), 103–129.

THORPE, S.A., HALL, A. & CROFTS, I. 1972 The internal surge in loch ness. *Nature* **237** (5350), 96–98.

TROWBRIDGE, J.H., HELFRICH, K.R., REEDER, D.B., MEDLEY, G.E., CHANG, M.-H., JAN, S., RAMP, S.R. & YANG, Y.-J. 2025 Observations of the bottom boundary layer beneath the world's largest internal solitary waves. *J. Geophys. Res.: Oceans* **130** (3), e2024JC022028.

VAUGHAN, N.J. & ZAKI, T.A. 2011 Stability of zero-pressure-gradient boundary layer distorted by unsteady klebanoff streaks. *J. Fluid Mech.* **681**, 116–153.

VERSCHAEVE, J.C.G. & PEDERSEN, G.K. 2014 Linear stability of boundary layers under solitary waves. *J. Fluid Mech.* **761**, 62–104.

ZAHEDI, S., AGHSAEE, P. & BOEGMAN, L. 2021 Internal solitary wave bottom boundary layer dissipation. *Phys. Rev. Fluids* **6** (7), 074802.

ZAKI, T.A. 2013 From streaks to spots and on to turbulence: exploring the dynamics of boundary layer transition. *Flow Turbul. Combust.* **91** (3), 451–473.

ZULBERTI, A., JONES, N.L. & IVEY, G.N. 2020 Observations of enhanced sediment transport by nonlinear internal waves. *Geophys. Res. Lett.* **47** (19), e2020GL088499–2020GL088499.

https://doi.org/10.1017/jfm.2026.12196 Published online by Cambridge University Press